Geomechanics and Engineering, *Vol. 37, No. 1 (2024) 73-84*
https://doi.org/10.12989/gae.2024.37.1.073

Stress and wear distribution characteristics of cutterhead for EPB shield tunneling in cobble-boulders

Zhiyong Yang*[1], Xiaokang Shao[1a], Hao Han[1b], Yusheng Jiang[1c], Jili Feng[1d],
Wei Wang[2e] and Zhengyang Sun[3f]

[1]*School of Mechanics and Civil Engineering, China University of Mining and Technology-Beijing, Ding, No. 11 Xueyuan Road, Haidian District, Beijing 100083, P.R. China*
[2]*China Railway Electrification Bureau Group Co., Ltd., Beijing 100036, China*
[3]*Beijing Urban Construction Group Co., Ltd., Beijing 100088, China*

(*Received May 29, 2023, Revised February 25, 2024, Accepted March 21, 2024*)

Abstract. Owing to the high strength and abrasive characteristics of cobble-boulders, cutters are easily worn and damaged during shield tunneling, making construction inefficient. In the present work, the stress on the ripper and scraper on the cutterhead was analyzed by the PFC3D–FLAC3D coupling model of shield tunneling to get insight into the performance of the cutterhead for cutting underground cobble and boulders. The numerical calculation results revealed that the increase in trajectory radius leads to a rising stress on the cutters, and the stress on the front cutting surface is greater than that on the back of the cutters. Moreover, the correlation between cutter wear and stress is revealed based on field measurement data. The distribution of the cutter stress is consistent with the cutter wear and breakage characteristics in actual construction, in which more extensive cutter stress is exhibited, extreme cutter wear appears, and more cutter breakage occurs. Finally, the relationship between the cutterhead opening area's layout and cutter wear distribution was investigated, indicating that the cutter wear extent is the most severe in the region where the radial opening ratio dropped sharply.

Keywords: cobble-boulder stratum; cutter stress; cutter wear; PFC3D–FLAC3D coupling; radial opening ratio; shield tunnel

1. Introduction

According to *the Code for Geotechnical Engineering Investigation* of China “GB50021-2019”, boulders are referred to as round or sub-round stones with particle sizes greater than 200 mm in soil. The underground cobble and boulder layers in the Beijing area are with the characteristics of large particle size, high strength, and strong abrasion. Thence, when excavating tunnels in this area, the tunneling efficiency is low due to the severe cutter wear of earth pressure balance (EPB) shields, and cutters often need to be renewed after short driving distances. Consequently, understanding the wear behavior of cutters during EPB shield tunneling in cobble and boulder is of vitality for improving construction efficiency and reducing construction costs.

In practice, the continuous friction between cutter and soil during the working of cutterhead causes the constant loss of material on the surface of cutter, which is the most common cutter wear phenomenon occurred in shield construction (Kwak and Ko 2022, Liu *et al.* 2022). However, in pebble and boulder formations with large grain sizes, cutter is more likely to collide with stone, which causes cutter damage (Mohammadi *et al.* 2016). Consequently, cutter wear can be considered as a superposition of frictional and impact fracture wear for cutter dealing with underground pebbles and boulders. So far much work has been focused on the factors influencing cutter wear and the model of cutter wear prediction. Bakar *et al.* (2021) conducted Laboratoire Central des Ponts et Chaussées (LCPC) tests on quartz and garnet with impellers of different material hardness and found that increasing impeller hardness decreases material deformation and slightly increases brittle fractures. Gharahbagh *et al.* (2013) studied the relation of cutter wear and abrasive of granular soils. Altan *et al.* (2018) investigated the influence of cutting parameters on various cutter wear regions on the cutter side. Mosleh *et al.* (2013) studied the effect of soil water content variation on cutter wear. Amoun *et al.* (2017) discussed the influence of geological parameters and tunneling factors on cutter wear. Regarding the cutter wear prediction model, on the other hand, Grasmick and Mooney (2021) adopted based geostatistics parameters to predict TBM cutter wear. Luo *et al.* (2005) used hard metal coated carbide cutting inserts to conduct cutter wear tests under different working conditions to predict the cutter surface wear area behind the cutter, Yang *et al.* (2021) proposed a

---

*Corresponding author, Associate Professor
E-mail: yangzy1010@126.com
[a]Ph.D. Student
[b]Ph.D. Student
[c]Professor
[d]Professor
[e]Ph.D. SN ENGR
[f]Ph.D. SN ENGR

http://www.techno-press.org/?journal=gae&subpage=7
ISSN: 2005-307X (Print), 2092-6219 (Online)

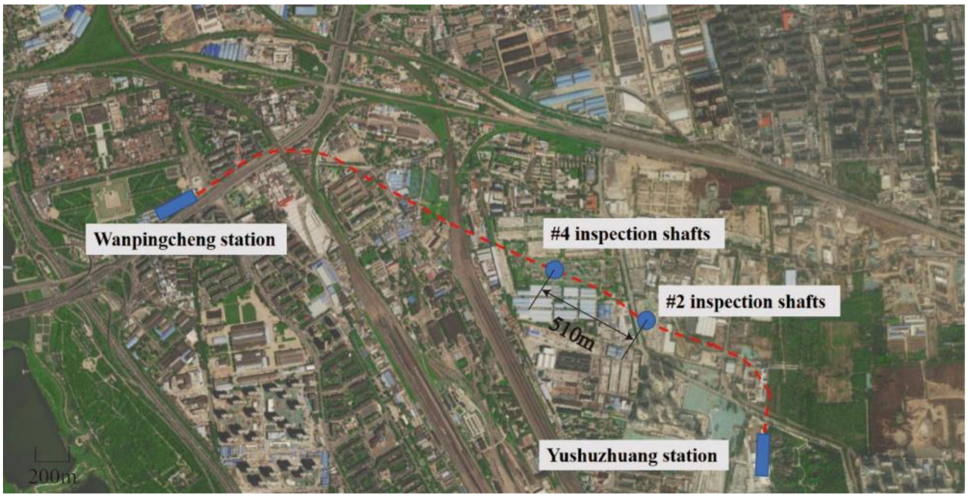

Fig. 1 Aerial view of Metro Line 16

wear coefficient selection method that is suitable for cutter wear calculation in composite strata. Li *et al.* (2017) quantitatively evaluated the feasibility of cutter wear to complete shield tunneling within a predetermined tolerance using the interval variable method. In addition, Toubhans *et al.* (2020) analyzed the change in the cutter cutting stress by conducting an in-depth study of the cutting phenomena and thus established a cutter cutting force model. Jiang *et al.* (2022) established the prediction model of tool wear by regression analysis of the measured data of cutterhead with a diameter of 9 meters.

The development of numerical simulation methods has extended the researchers' understanding of the working process of shield cutters so that nowadays many numerical simulations are used to identify and analyze the cutter stress distribution (Li *et al.* 2018, Zhu *et al.* 2017, Tao *et al.* 2021), among which discrete element methods (DEM) like PFC have been widely employed (Choi and Lee 2015, Han *et al.* 2017, Hu *et al.* 2021, Kim *et al.* 2022, Xu *et al.* 2021, Xue *et al.* 2021, Zhang *et al.* 2020, Zhu *et al.* 2020). In these work, the relationship between cutter penetration, spacing, rock strength, and joint and cutter stresses has been recognized while the cutter stress state during rock-breaking has also been revealed. However, these studies have focused more on disc cutters but little on the digging performance and cutter stress of spoke-type cutterhead as well as ripper and scraper, which are widely used in soft soil and sandy cobble formations. Moreover, the simulation of the full-size cutterhead rotation process is challenging due to the calculation scale limit of DEM. With these gaps in mind, coupling finite difference or finite element methods with DEM are naturally introduced to bypass the limit of alone DEM simulating scale in cutterhead tunneling process (Jiang *et al.* 2021, Labra *et al.* 2017), which are in fact excellent to model tunneling process under a wide range of ground conditions.

In previous studies, shield cutters' stress and wear characteristics have been paid much more attention under hard rock, soft soil, and sand ground conditions. Still, it is necessary to understand and explain the fracture-type mechanism of friction-collision interaction between spoke-type cutterheads and large-size stones in underground cobble-boulder layers because such complicated layers often meet in tunneling. In the present work, the PFC3D-FLAC3D coupling method is employed to study the tunneling process of EPB shield cutterhead in cobble-boulder based on the shield tunneling of Beijing Metro Line 16. The cutterhead working area was simulated using DEM, while the finite difference method evaluated the ground far from the tunnel face. Cutters' stress and wear characteristics were detailed by analyzing the cutter stress and actual cutter wear data at different project positions. The consequences of this work may be beneficial for the optimal design of shield cutters in tunneling under cobble-boulder ground.

2. Engineering geologic background

2.1 Engineering overview

The Yu-Wan section of Beijing Metro Line 16, located southwest of Beijing, was constructed using an EPB shield, launched at Yushuzhuang, and received at Wanpingcheng Station. The length of the tunnel is 2807.5 m, and an aerial view of the tunnel section is shown in Fig. 1. The tunnel adopts a reinforced concrete segment with an inner diameter of 5800 mm, an outer diameter of 6400 mm, and a ring width of 1200 mm. According to survey data, the underground in the region from the ground surface to bottom are plain fill, round gravel, #3 cobbles, #4 cobble-boulders, and clay rock. The buried depth of the tunnel in the Yu-Wan interval is 9.22–20.75 m. The shield mainly passes through the strata of #3 cobbles and #4 cobble-boulders, and it partially passes through the clay rock layer, and the groundwater level is below the tunnel floor.

2.2 Geological conditions of the section

This study deals with #2 and #4 inspection shafts in the left line of the tunnel, which are 1031 m and 1541 m, respectively, from the beginning of the Yushuzhuang station. All cutters were replaced at #2 inspection shaft and

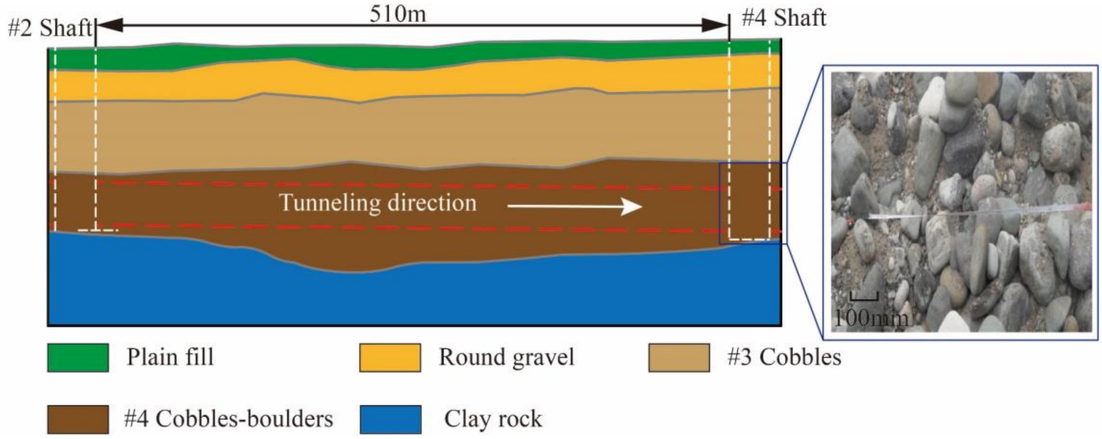

Fig. 2 Geological section of #2–#4 inspection shafts

Table 1 Cutter configuration parameters

Cutter type	Number	Height (mm)
Center cutter	1	400
#1 ripper	2	240
#2 ripper	32	175
#3 ripper	21	145
Scraper	78	120

their wear was measured after tunneling at #4 inspection shaft to analyze the wear characteristics. The geological conditions are shown in Fig. 2, in which the tunnel burial depth is 18–19 m and the shield crosses the soil of #4 cobble-boulders layer. The stratigraphic situation revealed by digging the shaft shows that the mass proportion of underground boulders (grain size 200–670 mm) in #4 soil layer is 48%, as shown in Fig. 2.

2.3 Cutterhead and cutter conditions

The EPB shield used in this tunnel is a spoke-type cutterhead composed of six spokes. The opening ratio of the cutterhead is 56%, and the excavation diameter is 6680 mm. The cutterhead is equipped with center cutters, rippers, scrapers, and a diameter retaining cutter. All cutter bodies are made of ultra-high strength steel (42CrMo), and the blade is made of tungsten steel alloy. The height of the central cutters is 400 mm, the layout height of ripper is divided into three layers with heights of 240 mm, 175 mm, and 140 mm, and the scraper height is 120 mm. All cutter parameters are listed in Table 1. The distribution of the rippers and scrapers on the spoke is shown in Fig. 3. An inner ring with a radius of 1820–1920 mm is used to improve the overall stiffness of the cutterhead.

3. PFC3D-FLAC3D modeling

In principle, PFC3D can simulate the mechanical behavior of cutter and soil particles on a mesoscopic level. However, the computational efficiency of PFC3D is relatively not high, which makes it difficult to be used to simulate the mechanical process of engineering problems. Whereas FLAC3D can characterize the macromechanical behaviors of the shield cutter and ground from the viewpoint of continuum mechanics, but it cannot take into account the contact-friction effect between soil particles and the cutter. In comparison, the PFC3D coupled with FLAC3D can readily be employed to simulate the mechanical behavior of the cutter and soil particles with less computational efforts, which will be detailed as follows.

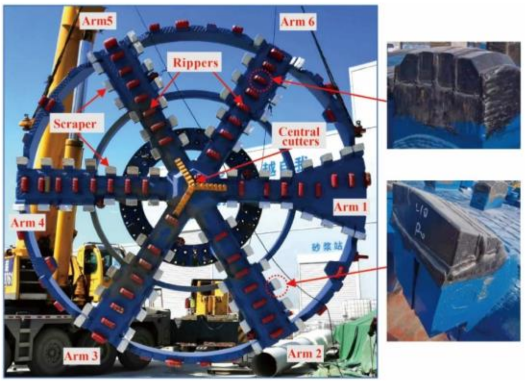

(a) Spoke-type cutterhead

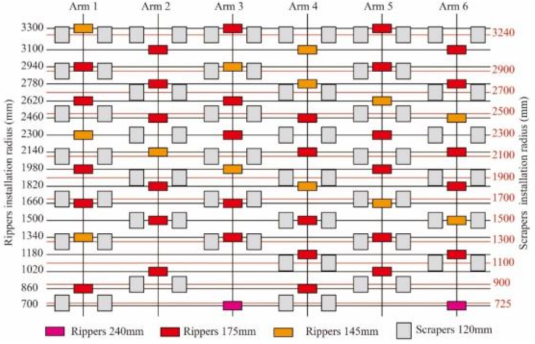

(b) Arrangement of rippers and scrapers on different spokes

Fig. 3 Cutterhead and cutter arrangement

3.1 Coupling principle

PFC3D-FLAC3D coupling technology can be implemented by three schemes, which cover one-

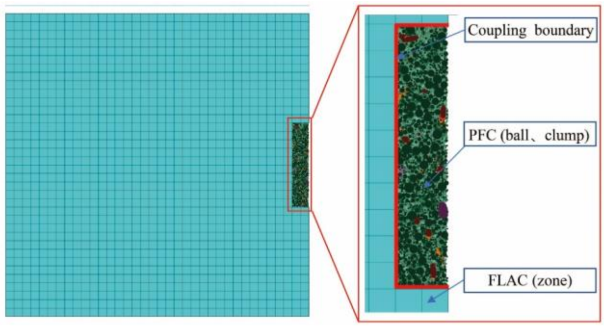

Fig. 4 The basic principle of coupling PFC3D–FLAC3D

dimensional structural element coupling, interface coupling, and superposition coupling. In the interface coupling, the zone element in FLAC3D is coupled with the balls, clumps, and pebbles in PFC3D. As shown in Fig. 4, the contact surface between the FLAC3D part and the PFC3D part is the coupling boundary (CB), in which coupling behavior occurs, while all the coupling data are transferred to each other through the CB. In the calculation process, PFC distributes the force or bending moment of the model elements (ball and clump) to each node of the boundary zone of FLAC3D equivalently through the CB. Moreover, FLAC3D also transfers the position or velocity of the zone surface on the boundary to the elements in the PFC3D model through the CB. The wall vertices on the CB can realize synchronous coupling motion with the grid points of the zone surface(Cai *et al.* 2007, Qu *et al.* 2019).

3.2 Cutterhead and cutter model

The spoke-type cutterhead was modelled with equal proportions, and the number, height, and position distribution of each cutter were consistent with the actual cutterhead. The geometry model was divided into many triangular grids, which were imported into PFC3D to generate wall units. As in actual shield tunneling, the shield shell was established to support the excavated soil, and a portal was introduced to maintain a lateral stratum.

3.3 Cobble-boulder particle model

The shapes of soil particles in cobble-boulders layer can be categorized into spheres, ellipsoids, and long ellipsoids. If the ball element in the PFC3D is adopted to mimic all the stone particles, the errors between the actual non-spherical stone and the model would be difficult to be ignored. Hence, the clump element was used to simulate the above three shapes of soil particles. In PFC3D, pebbles are divided into clumps and clusters, and whether they are destroyed is the main difference between the two pebbles. In the calculation process, the particles forming a clump have no relative deformation and will not be destroyed. A cluster is spheres bonded together by a certain strength, which is thought of as a combination of spherical particles. When the external force is sufficiently large, a cluster is destroyed. According to the strength test results of the boulder specimens taken from the site geological investigation, the uniaxial compressive strength of boulders is in the range of 177–448 MPa. Therefore, it is adequate to consider the large-size stones as unbreakable intact blocks. The muck discharge situation in the actual project also verifies this assumption that the vast majority of the boulder stones discharged from the soil chamber are still intact. Three typical boulder shapes were obtained using 3D scanning technology and then these data were imported into the Rhino program to provide the mesh and form clump templates. A suitable clump template was generated by changing the surface smoothness (D_i) and minimum to maximum particle radius ratio (R_a). By this way, the clumps formed by the superposition of spherical particles are close in shape to the geometric features of the actual stones (Cho *et al.* 2007, Cui *et al.* 2020). The parameters of the three types of clump templates are listed in Table 2.

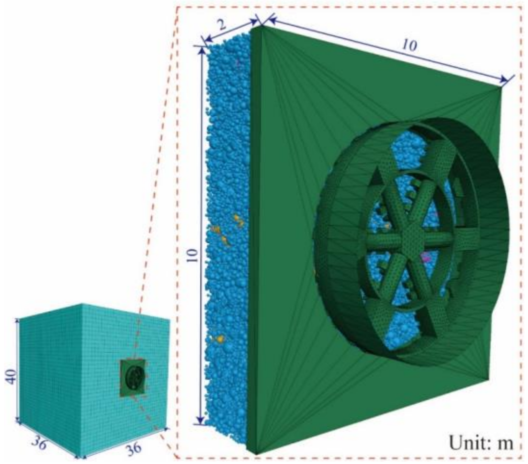

(a) Numerical model

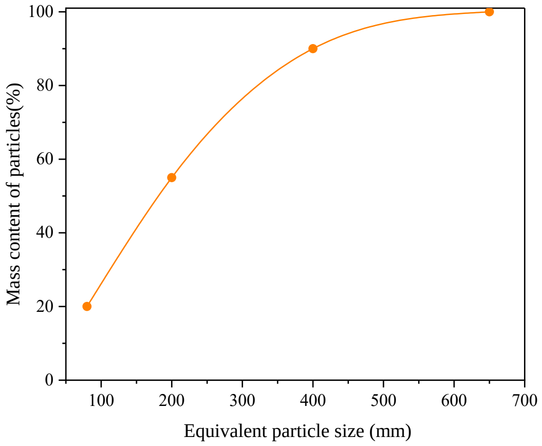

(b) Soil particle grading curve

Fig. 5 Computational model and equivalent particle size

In the modeling area, a size of 36 m × 36 m × 40 m, the computational domain was modelled by FLAC3D, among which the zone with the size of 2 m × 10 m × 10 m was excavated. Such excavated area that is composed by the cobble-boulders represented by the clump template. The size of sphere particles is in a range of 50–400 mm, with ellipsoid length of 400 mm and long ellipsoid length of 400–650 mm. Similar to the location where cobbles and boulders occur underground, the locations where the particles and clumps are generated are also randomly distributed. Still, the numerical model follows the principle

Table 2 Different types of clump particles

Shape of clump particles	Sphere	Ellipsoid	Long ellipsoid
Di	\	0.3	0.3
Ra	\	120	120
Number of pebbles	1	7	11
Cobbles and boulders			
Apparent shape	\	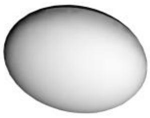	
Particle clump		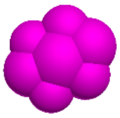	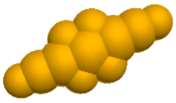

Note: D_i is surface smoothness, and *R*a represents maximum particle radius ratio

of the same content of stones of different particle sizes with the exploration results. The boundary conditions of the model were set to apply displacement constraints on the bottom and surroundings while the pressure was on the top to mimic the gravitational field action. The established geometry model and soil particle grading curve are shown in Fig. 5.

3.4 Parameter calibration

The contact models in PFC3D mainly include linear, linear bond, and parallel bond models. Because the particle cohesion in the boulders is small, the contact between pebbles can be described by a linear model. Further, it is difficult to be bonded soil particles in the boulders with the cutter so that the linear model is used to characterize the contact action between pebbles and the wall.

Since the microscopic parameters of DEM cannot directly reflect the macroscopic properties of soils, it is necessary to calibrate the DEM parameters via either inverse analyzing methods or numerical simulation tests. In the PFC3D simulation, FishTANK is widely employed to conduct a triaxial compression test to calibrate the mesoscopic parameters (Castro-Filgueira *et al.* 2017, Guo *et al.* 2013), which is also applied in the present study. Due to the fact that the shield tunnelling from #2 inspection shaft to #4 inspection shaft mainly passes through #4 cobble-boulders, the parameters of #4 cobble-boulders will be taken as a basic reference for convenience of calibration.

In the DEM experimental model with a height of 800 mm and diameter of 400 mm, by assigning different microscopic parameters to the model, the corresponding values of σ_1-σ_3 were obtained against the confining pressures σ_3 of 300 kPa, 400 kPa, and 500 kPa, respectively. From the σ_1-σ_3, the Mohr strength envelope could be drawn, from which the internal φ (friction angle) and c (cohesion) were gained. The microscopic parameters that are most consistent with the geological exploration report were obtained through repeated test calibration, and the stress–strain curves are shown in Fig. 6 (a). The Mohr stress circle and linear strength envelope are given in Fig. 6(b), where $c = -0.016$ and $\varphi = 40.92°$, which are basically identified with the geological exploration data $c = 0$ and $\varphi = 40°$. The calibrated particle effective modulus (E^*) is 500 MPa, the stiffness ratio (κ^*) is 2, and the friction coefficient (μ^*) is 2.5. In the FLAC3D simulated region, the Mohr–Coulomb model was used and the parameters were assigned according to the geological exploration result. The material parameters used in the FLAC3D simulation are listed in Table 3. The rationality of the mesoscopic parameters of the soil in the numerical simulation is judged by the consistency between its macroscopic mechanical properties and the actual test results, which also ensures the reliability of the simulation results.

Table 3 Material parameters used in simulation

Materials	H	B	S	C	ϕ	ν	ρ
	m	MPa	MPa	kPa	°	-	kg/m^3
Plain fill	0–2	13	10	0	10	0.2	1650
Round gravel	2–6	22	15	0	34	0.22	2100
#3 Cobble	6–15	41	28	0	38	0.22	2200
#4 Cobble-boulder	15–24	52	36	0	40	0.22	2250
Clay rock	24–36	22	14	40	35	0.24	2100

Note: H is the thickness of soil layer; B *and* G represent the bulk modulus and shear modulus of the soil layer, respectively (Ding *et al.* 2023); ν is poisson's ratio of the soil; C is cohesion of the soil; φ = internal friction angle of the soil; ρ is the weight of the soil

3.5 Simulation process

The implementation of PFC3D-FLAC3D coupling calculation is as follows:

(1) A thorough zone of model with a size of 36 m × 36 m × 40 m is described by FLAC3D except the excavation

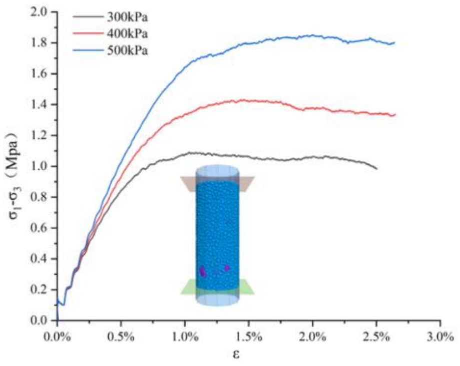

(a) stress–strain curves

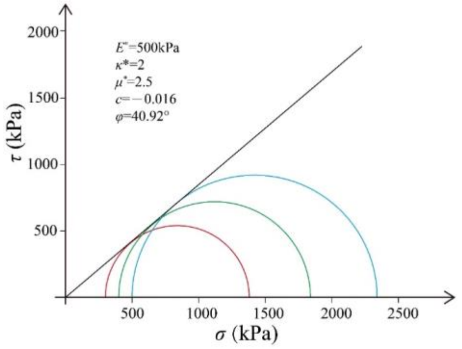

(b) Mohr circle and linear strength envelope

Fig. 6 Parameter calibration results

with a part of 2 m × 10 m × 10 m is simulated by PFC3D, as illustrated in Fig. 5.

(2) The coupling wall is positioned on the PFC3D–FLAC3D interface to transfer the force and displacement.

(3) The model applied gravity is to simulate the initial stress state for the initial balance.

(4) The cutterhead model in terms of some meshing methods like Rhino is imported into the PFC3D to generate the wall unit and regenerate the thorough cutterhead model that is usually with many triangular walls. The cutterhead is set with fast rotation speed to ensure that all the cutters entered the soil layer.

(5) After the cutterhead speed is cleared, the PFC3D model is rebalanced. Noted that the cutterhead and rotation speeds are the average values of the speeds from the inspection shafts of #2 and #4. The advance speed is 60 mm/min while the rotation speed was 1.2 r/min.

(6) To monitor the cutter stress, a FISH function is written to capture the normal contact force on the wall and wall triangle area, and then the pressure on the wall is obtained. The stress data of the cutterhead can be output for visual processing, and the average stress distribution of the cutterhead cutter tunneling at 50 mm is gained.

4. Discusstion of the numerical simulation results

4.1 Stress distribution of cutterhead

The stress distributions for the front and side of the cutterhead and each cutter are shown in Fig. 7. The stresses, 0–10 MPa, on the front and side of the cutterhead are relatively lower while the stresses near the inner ring increase. Especially at the intersection of the inner ring and the spokes, the maximum stress reaches 40 MPa. In addition, the stress on the spokes near the outer periphery of the cutterhead is high, i.e., up to 100 MPa. On the other hand, the cutter's stress levels on several areas are significantly higher.

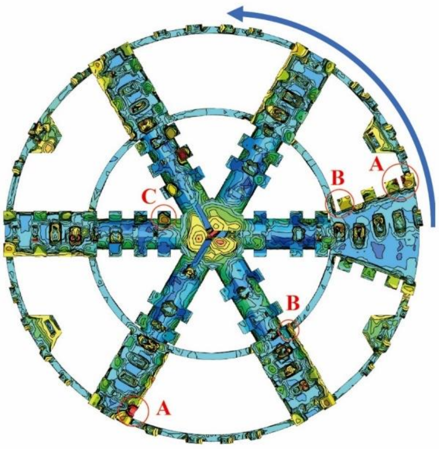

(a) front face

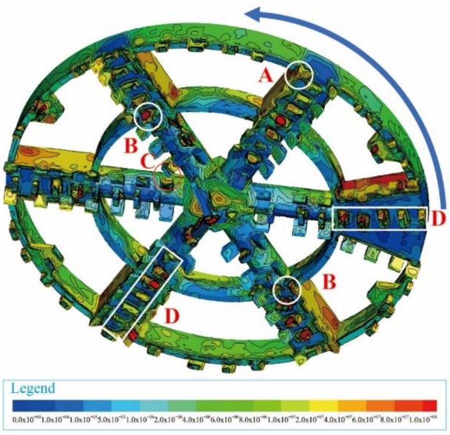

(b) side

Fig. 7 Stress nephogram of cutterhead and cutter (unit: Pa)

(1) area **A**: scraper near the periphery of the cutterhead;

(2) area **B**: ripper and scraper near the inner ring;

(3) area **C**: scraper near the center of the cutterhead;

(4) area **D**: cutting surface of the ripper outside the inner ring.

In areas **A**, **B**, and **C**, where the stress of the cutter is relatively large, these higher stresses have appeared at the junction of the cutter and center of the cutterhead, inner ring, or periphery, where the opening area is narrow. During cutting with the cutterhead, the slag soil flows into the chamber from the opening on the cutterhead. When the boulder flow space suddenly narrows relative to the cutterhead, it accumulates in the narrow opening area, increasing stress on the cutter.

In area D, each ripper outside the inner ring has a large installation radius and fast rotate speed, and its priority cuts cobble-boulders on the tunnel face; hence, the cutters' stress in this region is naturally significant.

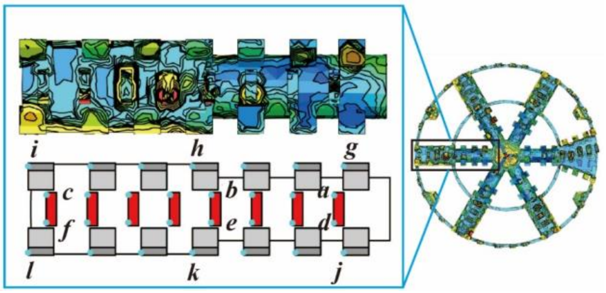

Fig. 8 #4 spoke beam cutter stress points and stress nephogram diagram

4.2 Ripper stress

To further understand the stress characteristics of the cutter, the ripper and scraper on the #4 spoke are selected for stress analysis. The stress monitoring position of the cutter is shown in Fig. 8 at the circular point. Fig. 9(a) shows the stress changes along with the tunneling distance from the ripper at six monitoring points. Among them, points ***a***, ***b***, and ***c*** are located at the back of the ripper, and points ***d***, ***e***, and ***f*** are situated on the active surface of the ripper cut soil. The stress on the cutting surface of the ripper is significantly greater than that on the back of the ripper at the same trajectory. To points ***a*** and ***d***, the trajectory radius is minimum; to points ***b*** and ***e***, it is located in the inner ring; and to points ***c*** and ***f***, it is maximum.

The average stress of the ripper on different trajectories on #4 spoke was selected to study its change along the trajectory radius, as shown in Fig. 9 (b). From Fig. 9(b), it is found that with an increase in the trajectory radius, the stress of the ripper has an overall increasing trend, and the fitting equation of the stress on the cutting surface of the ripper is as follows.

$$\sigma_1 = -24.8\times10^{-6}x^2 + 0.136x - 83.1 \tag{1}$$

$$R^2 = 0.865 \tag{2}$$

where σ_1 is the stress on the cutting surface of the ripper (unit: MPa), x represents the distance between the installation position of the ripper and the center of the cutterhead (unit: mm).

Inside the inner ring, the stress of the ripper increases rapidly, and the stress on the outer side of the inner ring does not increase significantly, all at approximately 100 MPa. The fitting equation of the stress on the back of the ripper is as follows

$$\sigma_1 = -7.6\times10^{-6}x^2 + 0.040x - 17.7, \tag{3}$$

$$R^2 = 0.718 \tag{4}$$

where σ_2 is the stress on the back surface of the ripper, meanings of x is references to Eq. (1).

The overall positive increase in cutter stress levels with an increase in their installation radius is mainly because the running speed of the cutter increases linearly with increasing radius, and faster cutting speeds result in tremendous kinetic energy of the collision. As a result, cutters with larger installation radii were subjected to more

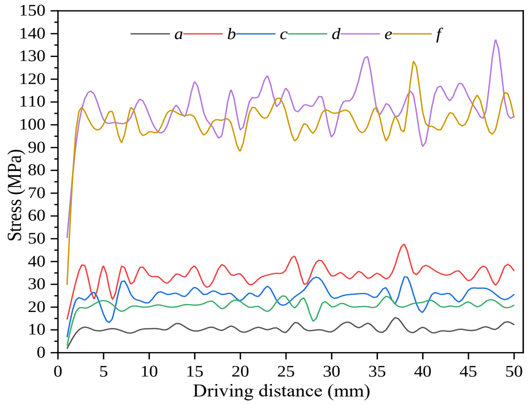

(a) Stress on the rippers during tunneling

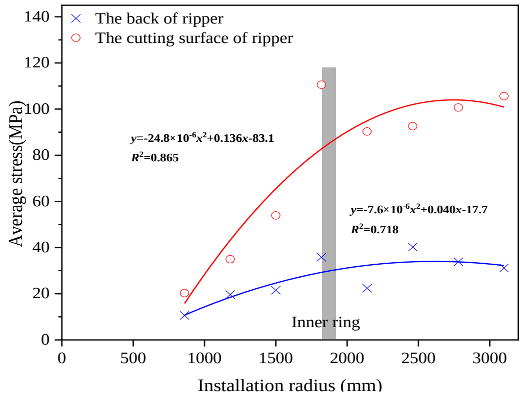

(b) Average stress on rippers at different trajectories radius

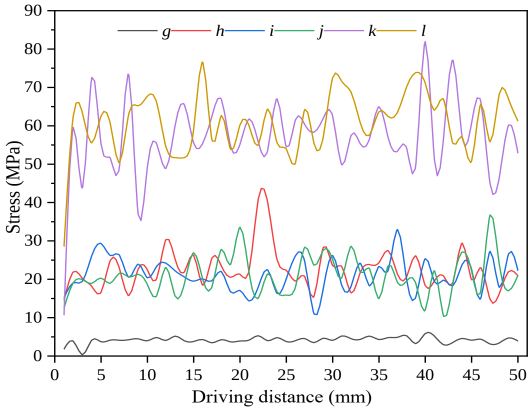

(c) Stress variation of scraper along tunneling distance

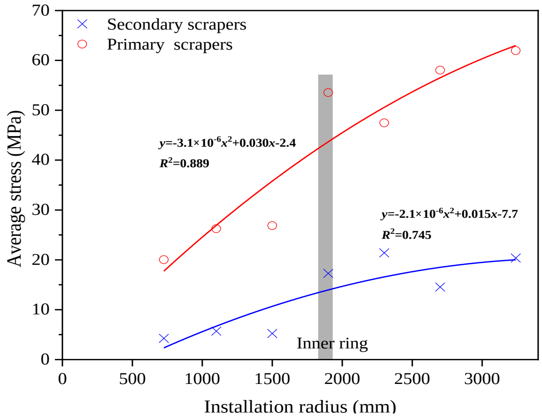

(d) Average receiving stress diagrams of scrapers on different path radii

Fig. 9 Cutting stresses

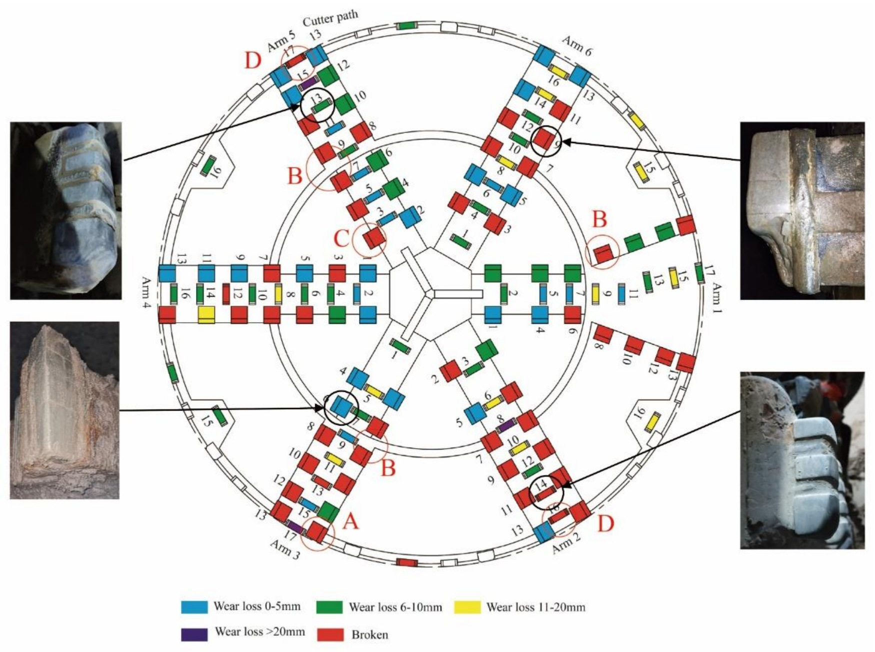

Fig. 10 Cutter wear distribution

substantial impact effects of underground stones and showed more severe wear. In addition, a unique phenomenon needs to be pointed out, i.e., the cutter stress near the inner ring is significantly higher than that of the other cutters. This is due to the restriction of the cutterhead opening, which increases the stone trajectory of entering the chamber and creates a stress concentration.

Compared with the cutting surface of the ripper, the increase in the back of the ripper is smaller. The stress on the cutting surface of the ripper is much larger than that on the back of the ripper, and the stress on the back of the ripper is less than 40 MPa, while the stress on the cutting surface of the ripper is up to 110 MPa.

4.3 Scraper stress

Fig. 9(c) shows the scraper stress changes at six monitoring points along with the cutterhead driving distance. The stress changes of the scraper are less volatile than those of the ripper, and the stress changes of the scraper are more prominent, where ***g***, ***h***, and ***i*** are located in the secondary scraper (on the backside of a spoke when the cutterhead rotates), and ***j***, ***k***, and ***l*** are located in the main scraper (on the front side of the spoke when the cutterhead rotates). The stress of the main scraper is significantly greater than that of the secondary scraper with the same trajectory. The trajectory radii of ***g*** and ***i*** are the smallest, ***h*** and ***k*** are located in the inner ring, and the trajectory radii of ***i*** and ***l*** are the largest. From the perspective of trajectory radius, the scraper stress with the smallest trajectory radius is the smallest. However, the scraper stress at the inner ring is not significantly different from that at the maximum trajectory radius.

The average value of the scraper stress on different trajectories is selected for analysis to study the change in the scraper stress along the trajectory radius. As shown in Fig. 9(d), the main and secondary scraper's stress-fitting equations are as follows.

$$\sigma_3 = -3.1\times10^{-6}x^2+0.030x-83.1 \tag{5}$$

$$R^2 = 0.889 \tag{6}$$

$$\sigma_4 = -2.1\times10^{-6}x^2+0.015x-7.7, \tag{7}$$

$$R^2 = 0.748 \tag{8}$$

where σ_3 and σ_4 are the stress on the main and secondary scraper, respectively; x represents the distance between the installation position of the scraper and the center of the cutterhead.

With an increase in the trajectory radius, the stress of the scraper increases, but the stress of the scraper in the inner ring increases sharply. The stress of the main scraper is much larger than that of the secondary scraper; the stress of the secondary scraper is less than 20 MPa and that of the main scraper is 20–65 MPa.

5. Characteristics of the cutter wear

5.1 Measurement of the cutter wear

To reveal the distribution of cutter wear on the cutterhead after tunneling, the residual height of each alloy block on each cutter was measured in the inspection shaft. The average difference between the original height and the residual height of all alloy blocks on the cutter is defined as the wear value. Similarly, the average of all cutters' wear value on the same trajectory is taken as the cutter wear of this trajectory. Moreover, cutter alloy blocks were found to be broken during the measurements, which is a unique phenomenon of shield tunneling in the boulder layer. To

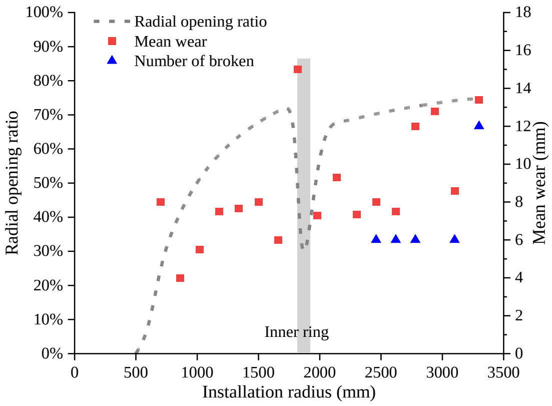

(a) rippers

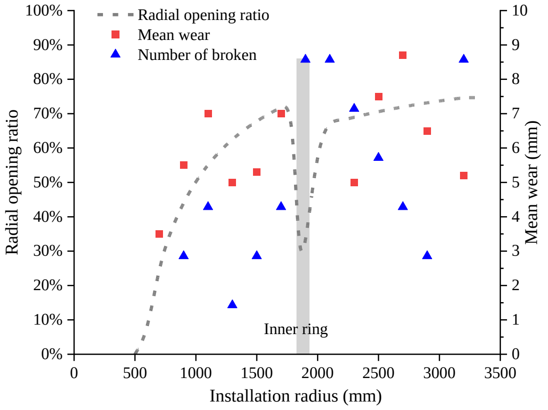

(b) scrapers

Fig. 11 Amount of wear and broken cutters at different trajectory radii

distinguish it from the normal cutter wear, the cutters with such broken alloy blocks are classified as broken. The distribution of cutter wear and breakage locations is shown in Fig. 10.

The wear extent and breakage of the rippers are distributed according to different trajectory radii, as shown in Fig. 11(a) (cutter wear amount in Fig. 11 is the average of all cutter wear in the same trajectory). The cutter wear generally increases with the increase of the trajectory radius. However, that of trajectory 8 (installation position of radius 1820 mm) is abnormally large, and the wear amount is the largest in this trajectory distribution. There are 55 rippers, and 6 damaged, representing damage of 10.9%, mainly distributed near the outer edge of the cutterhead.

The wear extent and damage of the scraper are distributed according to different trajectory radii, as shown in Fig. 11(b). There are 78 scrapers, and 43 damaged, representing damage of 55.1%. The number of breakages is the largest at trajectories 7 (radius 1700 mm), 8 (radius 1900 mm), and 13 (radius 3240 mm). A comparison of the number and arrangement of scrapers shows that all scrapers on trajectories 7 and 8 are damaged, and six of the 12 scrapers on trajectory 13 are damaged.

5.2 Correlation between cutter stress and wear

Comparing the stress distribution (Fig. 7) and the wear distribution of the cutter (Fig. 10), it is found that the areas

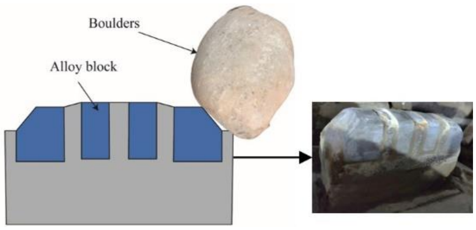

(a) Ripper

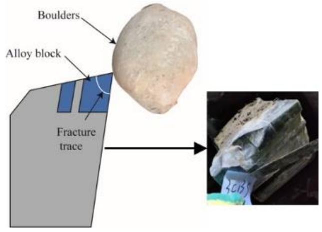

(b) Scraper

Fig. 12 Chart of impact between cutter and boulders

where the cutter is subjected to higher stresses tendency to have more increased wear or breakage, which also verifies the reliability of the simulation results. Only the ripper near the outer periphery of the cutterhead is broken, which corresponds to area **D** in Fig. 7, and the area where the ripper wears more corresponds to areas **B** and **D** in Fig. 7. The calculation results also show that the stress on the ripper near the outer periphery of the cutterhead is above 100 MPa, and the stress on the ripper at the circle in area B reaches 110 MPa. Therefore, there is a good correspondence between the stress on the ripper and the cutter's wear and breakage state. On the other hand, the scrapers are more broken than the rippers. The scrapers on areas **A**, **B**, and **C** in Fig. 7 correspond to a larger number of broken scrapers and a more significant amount of wear. There is also a good correspondence between the stress magnitude of the scrapers and the amount of cutter wear and breakage. The numerical simulation calculation results show a one-to-one correspondence between the stress concentration area and the cutter wear distribution, confirming the simulation results' reliability.

From the cutter stress results, the stress of the rippers is greater than that of the scraper with less damage (only 10.9%), and the amount of damage to the scrapers is greater (55.1%). This is mainly because the outer contour shapes of the two cutters are different. The rippers were designed with a shell shape, and the stress range is on a surface when the boulder collided with the rippers (as shown in Fig. 12(a)). Owing to a blade angle, the scraper's stress range is close to a point (Fig. 12(b)) when it collides with the cobble-boulders. Thus, the scrapers are more prone to damage when they collide with cobble-boulders. For the on-site cutter, most of the scrapers are damaged at the blade angle.

5.3 Influence of cutterhead opening area on cutter wear

The numerical simulation of the cutter stress nephogram diagram and the actual cutter wear shows that the cutter stress has a notable influence on the wear. In addition, whether the cobble-boulders can smoothly enter the soil

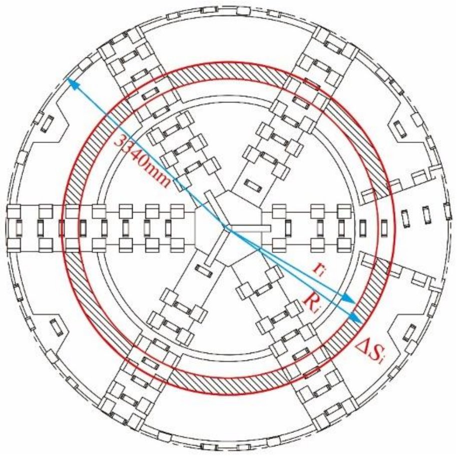

Fig. 13 Schematic diagram of radial opening ratio of cutterhead

chamber also dramatically influences the cutter wear. If it is difficult for the cobble-boulders to enter the soil chamber, they are squeezed in the narrow position of the cutter head. In this case, extended friction with the cutter causes severe cutter wear. Furthermore, cobble-boulders and repeated cutter collisions will be caused by cutter breakage. According to the studied shield tunnelling engineering, the vast majority of cobble-boulders are not broken. The cutterhead opening area also has a significant impact on cutter wear and damage.

5.3.1 Radial opening ratio of the cutterhead

The opening ratio of the cutterhead is an average index reflecting the overall condition of the cutterhead opening, which cannot describe the opening difference in different regions of the cutterhead. According to Yang *et al.* (2018), the characteristic curve of the radial opening ratio can be used to characterize the change in the opening along the radius of the cutterhead, reflecting the opening size of different regions on the cutterhead. This characteristic curve indicates that the cutterhead is divided into several equidistant rings according to a certain distance. After calculating the opening ratio of each ring, the curve was drawn with the radius of the cutterhead as the transverse axis and the annular opening ratio as the longitudinal axis. As shown in Fig. 13, the annular area S_i was calculated using Eq. (9), and the radial opening ratio K_i was calculated using Eq. (10),

$$S_i=\pi\left(R_i^2 - r_i^2\right) \tag{9}$$

$$K_i=\Delta S_i/S_i \tag{10}$$

where R_i is the outer radius of the ring, r_i is the inner radius of the ring, and ΔS_i is the annular opening area.

5.3.2 Correlation between radial opening ratio of the cutterhead and cutter wear

When calculating the radial opening ratio of a cutterhead, the entire cutterhead is divided into rings of equal width, and the width used in the division has an effect on the opening ratio curve. However, the selection of a suitable division width needs to be combined with engineering case. In the present study, the percentage of particles larger than 10 cm in the cobble-boulder layer is more than 70% so that selecting 10 cm as the division standard can effectively reflect the difficulty of cobble and boulder stones entering the soil chamber through the cutterhead opening. The correspondence between the radial opening ratio curve drawn according to this and the amount of cutter wear and the number of breakage is shown in Fig. 11.

From Fig. 11(a), the maximum wear of the rippers appears with the sharp drop in the radial opening ratio, where there is an inner ring in the cutterhead, and the radial opening ratio is small. The wear amount is 15 mm, which is much larger than that of the nearby rippers. This shows that the cutterhead opening has a significant influence on the wear degree of the rippers. Furthermore, Fig. 11(b) indicates that all six scrapers were damaged at the sharp decrease in the radial opening ratio, and the damage rate reaches 100%. The damage rate of these scrapers is much higher than that of the nearby scrapers, and the opening of the cutterhead has a significant influence on the damage of the scraper.

6. Conclusions

In this paper, a three-dimensional model of shield cutterhead tunneling in cobble-boulders has been established using the coupled PFC3D–FLAC3D method, with the motive of obtaining the stress distribution of the cutterhead during tunneling to provide a reference for cutter design and arrangement. In addition, cutter wear was measured after digging in the underground cobble-boulder layer, and a correlation between cutter wear and stress distribution was found. Furthermore, a structure evaluation parameter of the cutterhead was proposed, namely the radial opening ratio, and discovered its potential to be used to evaluate cutterhead opening design parameters and predict cutter wear distribution.

The numerical calculation results show that the cutter stress level exhibits an overall increasing tendency with a rising radius of the cutting trajectory. However, the cutter stress level near the inner ring of the cutterhead shows an abnormal increase. Its stress is much higher than the cutters in other areas, even higher than those with a larger radius of the outer cutting trajectory. Also, the distribution of the cutter opening was analyzed. It is found that the opening area at the intersection of the spokes and the cutterhead inner ring is narrow. After the cutter cut the boulders, it is difficult for the large stone to enter the soil chamber, resulting in increased stress on the cutter. In addition, the cutter wear distribution law for shield tunneling in such ground is revealed by actual wear measurement after tunneling. A high degree of consistency between cutter wear and stress calculation results is found, indicating that the cutterhead-soil model established by the coupled PFC3D–FLAC3D method can be used to evaluate the structural rationality of the cutterhead in underground cobble and boulder layer. The distribution of the cutterhead opening and the cutter position are the main factors determining the stress level of the cutter, which further influences the degree of cutter wear. Therefore, optimization of the cutterhead structure and opening configuration can be considered to enhance cutter life.

The size of the cutterhead opening affects whether the soil can enter the soil chamber smoothly during the excavation process and dramatically impacts the cutter's stress, wear, and breakage. In this paper, the radial opening ratio index is proposed, and its evaluation method matches better with the movement path of soil in front of the cutterhead than the overall cutterhead opening ratio, revealing the nature of cutter wear distribution on different installation radii. The results of numerical simulation and cutter wear analysis show that the tool stress is very high, and the cutter edge is prone to fracture when the shield is tunneling in the cobbles and boulders, which is very different from the normal cutter wear inhomogeneous ground. A special design of cutters for handling boulders is required to avoid the loss of tunneling efficiency caused by abnormal cutter damage. In particular, rippers and scrapers should have a more impact-resistant shell shape, a harder alloy block should protect scrapers on the blade, and the blade angle should be increased as much as possible to improve the impact resistance. Consequently, the radial opening ratio reduced area should be considered for some targeted optimization as far as possible to increase the number of cutters in the area or at least increase the amount of foam agent in the area during the tunneling process to improve the plasticity of the muck.

Acknowledgments

This research is supported by the National Natural Science Foundation of China (Grant No. U1261212), and the support is gratefully acknowledged.

References

Altan, E., Uysal, A. and Çaliskan, O. (2018), “Investigation into the effectiveness of cutting parameters on wear regions of the flank wear curve and associated cutting tool life improvement”, *Int. J. Mater. Prod. Tec.*, **57**(1-3), 54-70. https://doi.org/10.1504/IJMPT.2018.092931.

Amoun, S., Sharifzadeh, M., Shahriar, K., Rostami, J. and Azali, S.T. (2017), “Evaluation of tool wear in EPB tunneling of Tehran Metro, Line 7 Expansion”, *Tunn. Undergr. Sp. Tech*., **61**, 233-246. https://doi.org/10.1016/j.tust.2016.11.001.

Bakar, M.A., Majeed, Y., Rashid, M. and Ahmed, F. (2021), “Wear mechanisms of LCPC rock abrasivity test impellers of materials equivalent to TBM cutter head face tools”, *Tunn. Undergr. Sp. Tech.*, **116**, 104122. https://doi.org/10.1016/j.tust.2021.104122.

Cai, M., Kaiser, P., Morioka, H., Minami, M., Maejima, T., Tasaka, Y. and Kurose, H. (2007), “FLAC/PFC coupled numerical simulation of AE in large-scale underground excavations”, *Int. J. Rock Mech. Min. Sci*., **44**(4), 550-564. https://doi.org/10.1016/j.ijrmms.2006.09.01.

Castro-Filgueira, U., Alejano, L., Arzúa, J. and Ivars, D.M. (2017), Sensitivity analysis of the micro-parameters used in a PFC analysis towards the mechanical properties of rocks. In: ISRM European Rock Mechanics Symposium-EUROCK 2017. OnePetro,

Cho, N.a., Martin, C. and Sego, D. (2007), “A clumped particle model for rock”, *Int. J. Rock Mech. Min. Sci*., **44**(7), 997-1010. https://doi.org/10.1016/j.ijrmms.2007.02.002.

Choi, S.O. and Lee, S.J. (2015), “Three-dimensional numerical analysis of the rock-cutting behavior of a disc cutter using particle flow code”, *KSCE J. Civ. Eng.*, **19**, 1129-1138. https://doi.org/10.1007/s12205-013-0622-4.

Cui, S., Tan, Y. and Lu, Y. (2020), “Algorithm for generation of 3D polyhedrons for simulation of rock particles by DEM and its application to tunneling in boulder-soil matrix”, *Tunn. Undergr. Sp. Technol*., **106**, 103588. https://doi.org/10.1016/j.tust.2020.103588.

Ding, P., Shi, C., Tao, L., Liu, Z. and Zhang, T. (2023), “Research on seismic analysis methods of large and complex underground pipe structures in hard rock sites” , *Tunn. Undergr. Sp. Tech*., **135**, 105035.

Gharahbagh, E.A., Qiu, T. and Rostami, J. (2013), “Evaluation of granular soil abrasivity for wear on cutting tools in excavation and tunneling equipment”, *J Geotech Geoenviron*, **139**(10), 1718-1726. https://doi.org/10.1061/(ASCE)GT.1943-5606.0000897.

Grasmick, J. and Mooney, M. (2021), “A probabilistic geostatistics-based approach to tunnel boring machine cutter tool wear and cutterhead clogging prediction”, *J Geotech Geoenviron*, **147**(12), 05021014. https://doi.org/10.1061/(ASCE)GT.1943-5606.0002701.

Guo, J., Xu, G., Jing, H. and Kuang, T. (2013), “Fast determination of meso-level mechanical parameters of PFC models”, *Int. J. Min. Sci. Technol.*, **23**(1), 157-162. https://doi.org/10.1016/j.ijmst.2013.03.007.

Han, M., Cai, Z., Qu, C. and Jin, L. (2017), “Dynamic numerical simulation of cutterhead loads in TBM tunnelling”, *Tunn. Undergr. Sp. Tech.*, **70**, 286-298. https://doi.org/10.1016/j.tust.2017.08.028.

Hu, X., He, C., Walton, G. and Fang, Y. (2021), “Face failure in cobble-rich soil: Numerical and experimental approaches on 1 g EPB reduced scale model”, *Soils Found.*, **61**(6), 1500-1528. https://doi.org/10.1016/j.sandf.2021.08.008.

Jiang, B., Zhao, G.F., Gong, Q. and Zhao, X.B. (2021), “Three-dimensional coupled numerical modelling of lab-level full-scale TBM disc cutting tests”, *Tunn. Undergr. Sp. Tech*., **114**, 103997. https://doi.org/10.1016/j.tust.2021.103997.

Jiang, H., Zhu, J., Zhang, X., Zhang, J., Li, H. and Meng, L. (2022), “Wear mechanism and life prediction of the ripper in a 9-m-diameter shield machine tunneling project of the Beijing new airport line in a sand-pebble stratum”, *Deep Undergr. Sci. Eng*., **1**(1), 65-76.

Kim, Y., Hong, J., Shin, J. and Kim, B. (2022), “Shield TBM disc cutter replacement and wear rate prediction using machine learning techniques”, *Geomech. Eng.*, **29**(3), 249-258. https://doi.org/10.12989/gae.2022.29.3.249.

Kwak, N.S. and Ko, T.Y. (2022), “Machine learning-based regression analysis for estimating Cerchar abrasivity index”, *Geomech. Eng*., **29**(3), 219-228. https://doi.org/10.12989/gae.2022.29.3.219.

Labra, C., Rojek, J. and Onate, E. (2017), “Discrete/finite element modelling of rock cutting with a TBM disc cutter”, *Rock Mech. Rock Eng*., **50**, 621-638. https://doi.org/10.1007/s00603-016-1133-7.

Li, G., Wang, W., Jing, Z., Zuo, L., Wang, F. and Wei, Z. (2018), “Mechanism and numerical analysis of cutting rock and soil by TBM cutting tools”, *Tunn. Undergr. Sp. Tech.*, **81**, 428-437. https://doi.org/10.1016/j.tust.2018.08.015.

Li, X., Li, X. and Yuan, D. (2017), “Application of an interval wear analysis method to cutting tools used in tunneling shields in soft ground”, *Wear*, **392**, 21-28. https://doi.org/10.1016/j.wear.2017.09.010.

Liu, W., Yang, F., Zhu, X., Zhang, Y. and Gong, S. (2022), “Rock cutting behavior of worn specially-shaped PDC cutter in crystalline rock", *Geomech. Eng.*, **31**(3), 249-263. https://doi.org/10.12989/gae.2022.31.3.249.

Luo, X., Cheng, K., Holt, R. and Liu, X. (2005), "Modeling flank wear of carbide tool insert in metal cutting", *Wear*, **259**(7-12), 1235-1240. https://doi.org/10.1016/j.wear.2005.02.044.

Mohammadi, S., Firuzi, M. and Asghari Kaljahi, E. (2016), "Geological–geotechnical risk in the use of EPB-TBM, case study: Tabriz Metro, Iran", *Bull. Eng. Geol. Environ*., **75**, 1571-1583. https://doi.org/10.1007/s10064-015-0797-7.

Mosleh, M., Gharahbagh, E.A. and Rostami, J. (2013), "Effects of relative hardness and moisture on tool wear in soil excavation operations", *Wear*, **302**(1-2), 1555-1559. https://doi.org/10.1016/j.wear.2012.11.041.

Qu, T., Wang, S., Fu, J., Hu, Q. and Zhang, X. (2019), "Numerical examination of EPB shield tunneling–induced responses at various discharge ratios", *J. Perform. Constr. Fac*., **33**(3), 04019035.

Tao, L., Ding, P., Lin, H., Wang, H., Kou, W., Shi, C., Li, S. and Wu, S. (2021), "Three-dimensional seismic performance analysis of large and complex underground pipe trench structure", *Soil Dyn. Earthq. Eng*., **150**, 106904.

Toubhans, B., Fromentin, G., Viprey, F., Karaouni, H. and Dorlin, T. (2020), "Machinability of inconel 718 during turning: Cutting force model considering tool wear, influence on surface integrity", *J. Mater. Process. Tech.*, **285**, 116809.

Xu, H., Geng, Q., Sun, Z. and Qi, Z. (2021), "Full-scale granite cutting experiments using tunnel boring machine disc cutters at different free-face conditions", *Tunn. Undergr. Sp. Tech.*, **108**, 103719.

Xue, Y., Zhou, J., Liu, C., Shadabfar, M. and Zhang, J. (2021), "Rock fragmentation induced by a TBM disc-cutter considering the effects of joints: A numerical simulation by DEM", *Comput. Geotech.*, **136**, 104230.

Yang, Z., Jiang, Y. and Zhang, J. (2018), "Radial opening ratio of EPB TBM cutterheads", *Chinese J. Geotech. Eng*., **40**(12), 2312-2317. https://doi.org/10.11779/CJGE201812020.

Yang, Z., Sun, Z., Fang, K., Jiang, Y., Gao, H. and Bai, Z. (2021), "Cutting tool wear model for tunnel boring machine tunneling in heterogeneous grounds", *Bull. Eng. Geol. Environ*., **80**(7), 5709-5723.

Zhang, Z., Zhang, K., Dong, W. and Zhang, B. (2020), "Study of rock-cutting process by disc cutters in mixed ground based on three-dimensional particle flow model", *Rock Mech. Rock Eng*., **53**, 3485-3506.

Zhu, H., Panpan, C., Xiaoying, Z., Yuanhai, L. and Peinan, L. (2020), "Assessment and structural improvement on the performance of soil chamber system of EPB shield assisted with DEM modeling", *Tunn. Undergr. Sp. Tech*., **96**, 103092.

Zhu, X., Liu, W. and Lv, Y. (2017), "The investigation of rock cutting simulation based on discrete element method", *Geomech. Eng.*, **13**(6), 977-995. https://doi.org/10.12989/gae.2017.13.6.977.

GC